

Diffusion of lipids and GPI-anchored proteins in actin-free plasma membrane vesicles measured by STED-FCS

Falk Schneider^a, Dominic Waithe^b, Mathias P. Clausen^{a,c}, Silvia Galiani^a, Thomas Koller^a, Gunes Ozhan^{d,e}, Christian Eggeling^{a,b,*}, and Erdinc Sezgin^{a,*}

^aMRC Human Immunology Unit and ^bWolfson Imaging Centre Oxford, Weatherall Institute of Molecular Medicine, University of Oxford, Oxford OX39DS, United Kingdom; ^cMEMPHYS—Center for Biomembrane Physics, Department of Physics, Chemistry, and Pharmacy, University of Southern Denmark, 5230 Odense M, Denmark; ^dIzmir International Biomedicine and Genome Institute and ^eDepartment of Medical Biology and Genetics, Dokuz Eylul University Medical School, Inciralti-Balcova, 35340 Izmir, Turkey

ABSTRACT Diffusion and interaction dynamics of molecules at the plasma membrane play an important role in cellular signaling and are suggested to be strongly associated with the actin cytoskeleton. Here we use superresolution STED microscopy combined with fluorescence correlation spectroscopy (STED-FCS) to access and compare the diffusion characteristics of fluorescent lipid analogues and GPI-anchored proteins (GPI-APs) in the live-cell plasma membrane and in actin cytoskeleton-free, cell-derived giant plasma membrane vesicles (GPMVs). Hindered diffusion of phospholipids and sphingolipids is abolished in the GPMVs, whereas transient nanodomain incorporation of ganglioside lipid GM1 is apparent in both the live-cell membrane and GPMVs. For GPI-APs, we detect two molecular pools in living cells; one pool shows high mobility with transient incorporation into nanodomains, and the other pool forms immobile clusters, both of which disappear in GPMVs. Our data underline the crucial role of the actin cortex in maintaining hindered diffusion modes of many but not all of the membrane molecules and highlight a powerful experimental approach to decipher specific influences on molecular plasma membrane dynamics.

Monitoring Editor

Robert G. Parton
University of Queensland

Received: Jul 22, 2016

Revised: Mar 31, 2017

Accepted: Apr 4, 2017

INTRODUCTION

The cellular plasma membrane is a heterogeneous structure composed of various types of lipids and proteins, and this heterogeneity plays crucial roles in cellular signaling (Simons and Gerl, 2010; Sezgin *et al.*, 2017). The underlying physicochemical principles have been extensively studied (Lingwood and Simons, 2010; Sezgin *et al.*,

2017). A first comprehensive concept to describe the membrane structure and dynamics was the fluid mosaic model of Singer and Nicolson (1972), which suggested a homogeneous multicomponent system in which, in the long range, processes are based on free Brownian motion, yet, in the short range, interactions of lipids and proteins can form small-scale heterogeneous complexes. Later models suggested a more elaborate suborganization of the membrane into functional domains (Simons and Ikonen, 1997). These nanodomains, referred to as membrane rafts, were proposed to be enriched in cholesterol and saturated lipids (Simons and Ikonen, 1997) and be highly dynamic (Pike, 2006; Sezgin *et al.*, 2015b). Besides the relatively general raft concept, nanoclusters of specific membrane components have been reported. Glycophosphatidylinositol-anchored proteins (GPI-APs; Varma and Mayor, 1998), ganglioside GM1 (Yuan and Johnston, 2001), sphingomyelin (Guyomarc'h *et al.*, 2014), and specific immune receptor clusters (Dustin and Groves, 2012) are examples shown to build up nanoscale heterogeneous structures in the plasma membrane (Saka *et al.*, 2014).

This article was published online ahead of print in MBoc in Press (<http://www.molbiolcell.org/cgi/doi/10.1091/mbc.E16-07-0536>) on April 12, 2017.

The authors declare no conflict of interest.

*Address correspondence to: Erdinc Sezgin (erdinc.sezgin@rdm.ox.ac.uk), Christian Eggeling (christian.eggeling@rdm.ox.ac.uk).

Abbreviations used: FCS, fluorescence correlation spectroscopy; GPI-AP, glycosylphosphatidylinositol-anchored protein; GPMV, giant plasma membrane vesicle; GUV, giant unilamellar vesicle; STED, stimulated emission depletion.

© 2017 Schneider *et al.* This article is distributed by The American Society for Cell Biology under license from the author(s). Two months after publication it is available to the public under an Attribution–Noncommercial–Share Alike 3.0 Unported Creative Commons License (<http://creativecommons.org/licenses/by-nc-sa/3.0>).

"ASCB®," "The American Society for Cell Biology®," and "Molecular Biology of the Cell®" are registered trademarks of The American Society for Cell Biology.

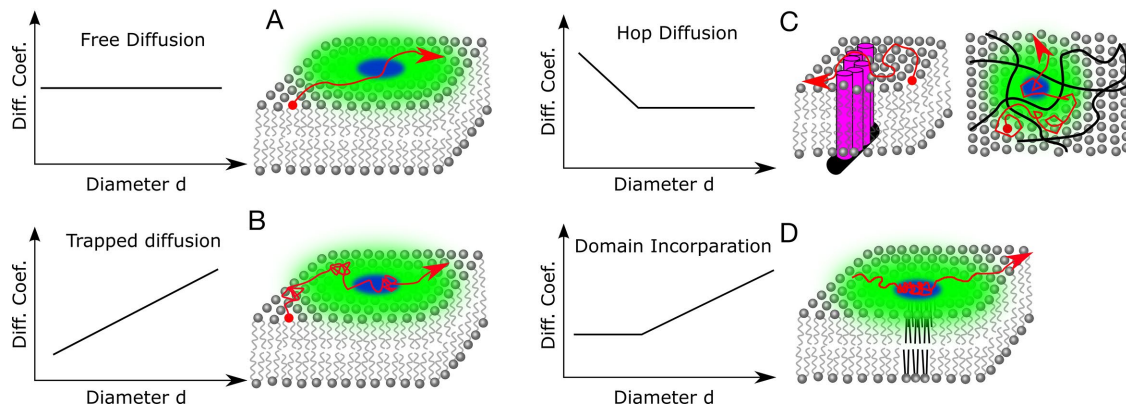


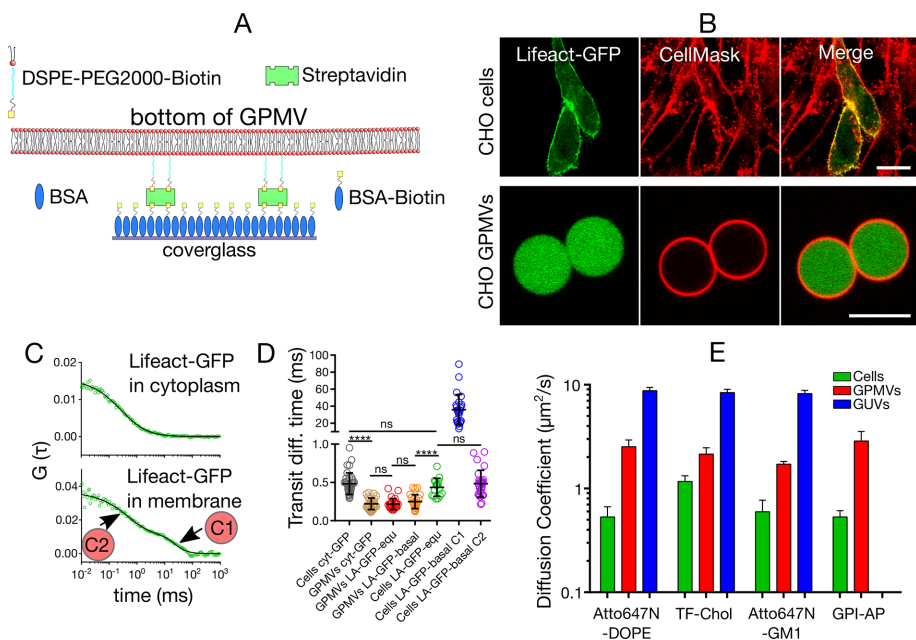
FIGURE 1: Possible diffusion modes in the cellular plasma membrane revealed by (left) determination of the apparent diffusion coefficient (D , Diff. Coef.) for different values of observation spot diameter (d) and (right) the potential molecular mechanisms behind these diffusion modes (red, molecular diffusion track; green and blue, large confocal and small STED microscope observation spots, respectively; gray, lipids; black, actin cytoskeleton; purple, actin-anchored transmembrane proteins). (A) Free diffusion; D remains constant. (B) Trapped diffusion; D decreases with decreasing d , presumably due to transient binding to immobile or slow-moving interaction partners, possibly assisted by the actin cytoskeleton. (C) Hop diffusion; D increases toward small d due to compartmentalization of the membrane by the cortical actin meshwork and transmembrane proteins associated with it, leading to fast diffusion inside the compartments as probed at small d and hindrance in crossing from one to the next compartment as observed at large d . (D) Transient domain incorporation; D decreases toward smaller d in a similar manner as in the trapping diffusion but levels out or slightly increases as the spot size gets closer to the domain size because diffusion is slowed down inside the domains, due, for example, to an increased molecular order.

Although the existence of rafts as a general organizing concept of the plasma membrane is under debate (Klotzsch and Schuetz, 2013; Sezgin *et al.*, 2015a, 2017), there is a consensus on the presence of membrane heterogeneity in terms of structure and dynamics (Sezgin *et al.*, 2015b). The temporal heterogeneity, for instance, is often quantitatively investigated by measuring diffusion of proteins and lipids in the cellular plasma membrane. Such diffusion measurements were used to determine the molecular mobility in segregated domains (Kahya *et al.*, 2003; Sezgin and Schwille, 2012), elucidate the binding dynamics of cell surface receptors (Yu *et al.*, 2009), and investigate the influence of the underlying cytoskeleton structure on membrane dynamics (Kusumi *et al.*, 2005, 2010; Mueller *et al.*, 2011; Andrade *et al.*, 2015; Fujiwara *et al.*, 2016; Koster and Mayor, 2016; Koster *et al.*, 2016) and the formation of transient interactions (Eggeling *et al.*, 2009; Honigsmann *et al.*, 2014), to name just some applications.

An important tool to measure molecular mobility in membranes is fluorescence correlation spectroscopy (FCS; Fahey *et al.*, 1977; Schwille *et al.*, 1999). In FCS, an apparent diffusion coefficient, D , is determined from the average transit time of fluorescently tagged molecules moving into and out of a microscope's observation spot. FCS data recorded for different observation spot sizes demonstrated that different components of the plasma membrane diffuse not only with different velocities but also with different diffusion modes (Wawrezynieck *et al.*, 2005; Eggeling *et al.*, 2009). The diffusion mode defines how the apparent diffusion coefficient of molecules changes with the size of the observation spot (Eggeling, 2015). Figure 1 illustrates proposed diffusion modes and their possible underlying mechanisms. For a molecule undergoing free (Brownian) diffusion, the apparent diffusion coefficient is not dependent on the size of the observation spot (Figure 1A). This is different for hindered diffusion; for example, D will decrease with decreasing observation spot size diameter, d , if molecules are transiently immobilized or trapped in, for example, immobile or slow-moving molecular com-

plexes (Figure 1B; Eggeling *et al.*, 2009; Mueller *et al.*, 2011). On the other hand, D will increase toward smaller d when molecules undergo hop or compartmentalized diffusion (Figure 1C; Fujiwara *et al.*, 2002; Clausen and Lagerholm, 2013; Andrade *et al.*, 2015). In case molecules are transiently incorporated into domains where their diffusion is slowed, D will decrease toward smaller d in a similar manner as for trapped diffusion but will level out or slightly increase again as d gets closer to the diameter of the domain size (Figure 1D; Honigsmann *et al.*, 2013; Guzman *et al.*, 2014; Sachl *et al.*, 2016). As outlined, the $D(d)$ dependence is usually determined by measuring FCS data for different observation sizes (spot-variation FCS; He and Marguet, 2011). This can be done either on conventional confocal microscopes with diffraction-limited observation spots with $d > 200$ nm (Wawrezynieck *et al.*, 2005) or on a superresolution stimulated emission depletion (STED) microscope with $d < 200$ nm (Eggeling *et al.*, 2009). The latter has the advantage of measuring the diffusion closer to the length scales of the features causing hindrances.

The diffusion mode of membrane molecules is a powerful indicator of their interaction dynamics and their bioactivity. Specifically, lipids may serve as signaling modulators for proteins with which they interact. For example, various membrane proteins have specific binding motifs for cholesterol (Schwarzer *et al.*, 2014), gangliosides (Coskun *et al.*, 2011), or sphingomyelin (Contreras *et al.*, 2012), which are crucial for the functionality of these proteins. Further, lateral diffusion of an active interferon- γ receptor is modulated by sphingomyelin and cholesterol, whereas that of an inactive mutant of this receptor is confined by the actin cytoskeleton (Blouin *et al.*, 2016). In addition, molecular simulations have shown a strong dependence of the conformation of proteins on the surrounding lipid membrane's dynamics (Polley *et al.*, 2017). Therefore exact determination of the diffusion modes of lipids and elucidation of their underlying regulatory principles offer crucial insights into the organization and functionality of membrane lipids and proteins. Unfortunately,



brane components but lack the actin cytoskeleton (Baumgart *et al.*, 2007). Our data underline the crucial role of the actin cortex in maintaining hindered diffusion modes of most but not all membrane molecules because hindered diffusion is to a large extent abolished in actin-free GPMVs. The use of STED-FCS on GPMVs constitutes a powerful experimental approach to investigate nanoscale lipid and protein dynamics in an isolated plasma membrane environment.

RESULTS

Measurements in cells and GPMVs

All of our measurements were performed on live adherent PtK2 or CHO cells and on GPMVs generated therefrom. The generation of GPMVs was induced using paraformaldehyde (PFA)/dithiothreitol (DTT) following a well-established protocol (Sezgin et al., 2012a). To exclude PFA/DTT-specific artifacts, we also tested GPMVs formed using *N*-ethylmaleimide (NEM), which gave similar results on diffusion of molecules (Supplemental Figure S1). SNAP- or fluorescently-tagged GPI-APs were expressed in the cells before GPMV formation. Fluorescently tagged lipids were incorporated into the GPMV membrane at relatively low concentrations after formation. One artifact that could potentially cause inaccuracies in diffusion measurements is the presence of molecules stuck to the glass coverslip. To eliminate this possibility and confirm proper plasma membrane incorporation of the fluorescent lipid analogues, we trypsinized the cells after treatment with lipid analogues as

the exact mechanisms causing the diffusion modes of lipids and proteins could not be unequivocally resolved. For example, trapped diffusion is believed to be caused by transient interactions with extremely slow or immobile membrane components (their exact identity being undiscovered) and to be assisted by cholesterol and the actin cytoskeleton (Figure 1B; Eggeling *et al.*, 2009; Mueller *et al.*, 2011). Hop diffusion is proposed to be induced by confinement from the cortical actin cytoskeleton meshwork and transmembrane proteins associated with it (Figure 1C; Ritchie *et al.*, 2003; Kusumi *et al.*, 2010; Andrade *et al.*, 2015). The domains into which molecules could transiently incorporate may follow the lipid raft idea (Wawrezinieck *et al.*, 2005). Many of these proposals were obtained from experiments using cell-perturbing drugs, such as cholesterol-oxidizing drugs or those depolymerizing the actin cytoskeleton. Yet the action of these drugs might be manifold. Therefore experiments under more-controlled conditions and in minimal systems containing only the essential elements are necessary to confirm the molecular mechanisms inducing the different hindrances in diffusion.

In this study, we use STED-FCS to compare the diffusion modes of fluorescently labeled lipids and GPI-anchored proteins (GPI-AP) in the plasma membrane of live cells and cell-derived membrane vesicles, so-called giant plasma membrane vesicles (GPMVs). Despite having their own artifacts caused by chemical vesiculation, GPMVs display an excellent model of the cellular membrane (Scott and Maercklein, 1979) because they contain most of the natural mem-

described previously (Chinnappen *et al.*, 2012). The time-lapse images confirmed that the signal originated from the cell membrane but not from molecules bound to the coverslip or to the cell surface proteins (Supplemental Figure S2). Measurements were carried out at room temperature, which minimized internalization of the fluorescent molecules and thus background signal (Eggeling *et al.*, 2009). We measured cells for not longer than 45 min at room temperature, during which the cells remained healthy. Moreover, representative results from diffusion mode measurements obtained at 37°C were similar to those obtained at room temperature (Supplemental Figure S3). We also carefully investigated the miscibility transition temperature of GPMVs to avoid artifacts resulting from phase separation at room temperature (Supplemental Figure S4). Finally, GPMVs were still mobile, making some of the measurements, especially the acquisition of 10- to 30-s FCS data, challenging. Hence we immobilized GPMVs by incorporating a small amount of lipids with a biotinylated PEG linker into the membrane of GPMVs and depositing them on a streptavidin-functionalized microscope coverglass surface (Figure 2A). We confirmed that immobilization did not influence the molecular diffusion in the membrane of the GPMVs by comparing FCS data obtained at the basal and apical membrane of immobilized GPMVs and of rarely appearing, nonmoving, non-immobilized GPMVs (Supplemental Figure S5). In the following, we determine molecular diffusion at the basal membrane of the immobilized GPMVs because it yielded the most reproducible

measurements due to the high-numerical aperture (NA) oil objective we applied for STED-FCS experiments.

GPMVs lack organized cytoskeleton

We first probed the organization of actin in the GPMVs to confirm the lack of actin cytoskeleton in these vesicles. We visualized the actin organization in adherent and suspended cells and in GPMVs derived therefrom. Figure 2B shows the filamentous actin (F-actin) organization in live adherent CHO cells expressing Lifeact–green fluorescent protein (Lifeact-GFP; a versatile fluorescence marker that transiently binds F-actin in living cells), where the cortical actin cytoskeleton is clearly visible as a bright structure beneath the plasma membrane (Clausen *et al.*, 2017). In contrast, in the CHO cell-derived GPMVs, we observed no such cortical actin network underneath the membrane; instead, actin was homogeneously distributed inside the GPMVs (Figure 2B). Similarly, monomeric actin (or globular actin [G-actin], labeled with the fluorescent protein citrine) localized primarily to the cell cortex, whereas it was homogeneously distributed inside the GPMVs (Supplemental Figure S6A). To unambiguously exclude the formation of a membrane-associated assembled cortical actin cytoskeleton in the GPMVs, we performed confocal FCS measurements for Lifeact-GFP in the cytosol (distant from the membrane, in the equatorial plane) and within the cortical actin cytoskeleton (at the plasma membrane, in the basal plane) of living CHO cells. The average transit times of Lifeact-GFP through the observation spot differed for cells and GPMVs. In cells, diffusion was equally fast in the cytosol as well as for one of the components at the basal plane, whereas another component at the basal plane exhibited a significantly reduced mobility, as expected within the intact cortex, where Lifeact-GFP transiently binds F-actin (Figure 2, C and D). Control experiments with free cytoplasmic GFP (cyt-GFP) confirmed that the first component resembles the free cytosolic Lifeact-GFP (Figure 2D). In GPMVs, mobility was equally fast for cyt-GFP and Lifeact-GFP in the equatorial plane and in the basal membrane. Disappearance of the slow component (component C1 in Figure 2C) in GPMVs indicates that only purely free Lifeact-GFP is present in the vesicles. It is worth noting that the cytosolic diffusion was relatively faster in GPMVs than in live cells, presumably due to the absence of organelles and cytoskeletal elements (e.g., microtubules), which causes a less crowded environment within the GPMVs. Finally, we treated GPMVs with the F-actin–depolymerizing drug latrunculin B, which would disrupt any remaining cortical actin structures; yet we observed no significant differences in lipid mobility between latrunculin-treated and untreated GPMVs (Supplemental Figure S6B). In conclusion, we confirmed that the cortical actin cytoskeleton was abolished in GPMVs.

Mobility of lipids in cells, GPMVs, and GUVs

Cortical actin has tremendous effect on the membrane structure and dynamics, which are usually elucidated using actin-targeting drugs (Kusumi *et al.*, 2010; Mueller *et al.*, 2011; Koster and Mayor, 2016; Koster *et al.*, 2016; Saha *et al.*, 2016). To understand the effect of complete absence of the actin cortex on molecular diffusion in membranes, we tested the mobility of fluorescent (Atto647N- or TopFluor-labeled) analogues of an unsaturated phospholipid (Atto647N-1,2-dioleoyl-sn-glycero-3-phosphoethanolamine [DOPE]), cholesterol (TF-Chol), and the glycolipid GM1 (Atto647N-GM1) in the plasma membrane of live CHO cells, in GPMVs derived therefrom, and in artificial free-standing giant unilamellar vesicles (GUVs; 100% 1,2-dioleoyl-sn-glycero-3-phosphocholine [DOPC]). We applied confocal FCS to determine average diffusion coefficients of these analogues.

Diffusion of all tested lipid analogues was significantly faster in GPMVs than in living cells but still significantly slower than in the GUVs (Figure 2E). The difference in diffusion between cells and GPMVs is presumably due to the lack of the actin cortex in GPMVs; hindrance due to the actin-mediated compartmentalization (Fujiwara *et al.*, 2016) is likely to be abolished in GPMVs. The difference between the GUVs and GPMVs can be attributed to less molecular crowding in GUVs due to the absence of proteins (Houser *et al.*, 2016). All tested molecules diffused with similar diffusion coefficients in GUVs ($D \approx 8.5 \mu\text{m}^2/\text{s}$). In live cells, Atto647N-DOPE and Atto647N-GM1 had similar diffusion coefficients ($D \approx 0.5 \mu\text{m}^2/\text{s}$), whereas TF-Chol was notably faster ($D \approx 1.2 \mu\text{m}^2/\text{s}$), in accordance with previous findings (Solanko *et al.*, 2013; Hiramoto-Yamaki *et al.*, 2014). Yet, in GPMVs, Atto647N-DOPE and TF-Chol had similar diffusion coefficients ($D \approx 2.5 \mu\text{m}^2/\text{s}$). The larger increase in mobility from live cells to GPMVs for Atto647N-DOPE compared with TF-Chol suggests a stronger confinement of the phospholipid analogue by the cortical actin cytoskeleton than of cholesterol. In comparison, diffusion of Atto647N-GM1 increased only threefold from $D \approx 0.5 \mu\text{m}^2/\text{s}$ in live cells to $D \approx 1.5 \mu\text{m}^2/\text{s}$ in GPMVs, which highlights that hindrances in diffusion of the GM1 analogue seems to be less associated with the actin cortex.

Hindered diffusion in cells and GPMVs

Hindered diffusion in the plasma membrane of intact living cells has been reported several times for lipid analogues—specifically, trapped diffusion in the case of sphingomyelin or GM1 (Eggeling *et al.*, 2009; Mueller *et al.*, 2011; Sezgin *et al.*, 2012b) and hop diffusion in the case of phospholipids such as DOPE (Fujiwara *et al.*, 2002; Clausen and Lagerholm, 2013; Andrade *et al.*, 2015). We investigated whether these hindered diffusion modes are present also in GPMVs. Using STED-FCS, we tested the diffusion modes of four different lipid analogues, all labeled with the organic dye Atto647N: a saturated (Atto647N-1,2-dipalmitoyl-sn-glycero-3-phosphoethanolamine [DPPE]) and an unsaturated (Atto647N-DOPE) phospholipid, as well as sphingomyelin (Atto647N-SM) and the ganglioside GM1 (Atto647N-GM1). As outlined in Figure 1, STED-FCS measurements allow us to determine the dependence of the apparent diffusion coefficient, D , on the diameter of the microscope's observation spot, d , elucidating the nanoscale diffusion mode.

In cells, Atto647N-DPPE diffused freely (Figure 3, A and B, as expected for PtK2 cells; Eggeling *et al.*, 2009), whereas we found two pools (P1 and P2) of differently diffusing Atto647N-DOPE lipid (Figure 3, C and D). Varying between individual cells or even different positions on the same cell, we found either characteristics of free diffusion (P2, ~60% of the cases) or slight hop diffusion (P1, ~40% of the cases), which underlines the large heterogeneity in the cellular membrane organization. Atto647N-SM showed trapped-like diffusion in cells (Figure 3, E and F), as shown previously for PtK2 cells (Eggeling *et al.*, 2009).

In GPMVs, diffusion of the DOPE, DPPE, and SM analogues turned free with approximately fivefold-increased mobility (Figure 3, A, C, and E). The abolition of hindered diffusion in GPMVs is further highlighted by plotting the ratio $D_{\text{STED}}/D_{\text{Conf}}$ of the apparent diffusion coefficients. D_{STED} and D_{Conf} were determined from the FCS recordings with maximum and zero STED laser power, respectively (Figure 3A, black boxes). $D_{\text{STED}}/D_{\text{Conf}} = 1$ indicates free, $D_{\text{STED}}/D_{\text{Conf}} > 1$ hop, and $D_{\text{STED}}/D_{\text{Conf}} < 1$ trapped diffusion. In cells, we found $D_{\text{STED}}/D_{\text{Conf}} \approx 1$ for Atto647N-DPPE (Figure 3B), as well as for one pool of Atto647N-DOPE (P2; Figure 3D), $D_{\text{STED}}/D_{\text{Conf}} \approx 1.8$ for the other pool of Atto647N-DOPE (P1; Figure 3D), and

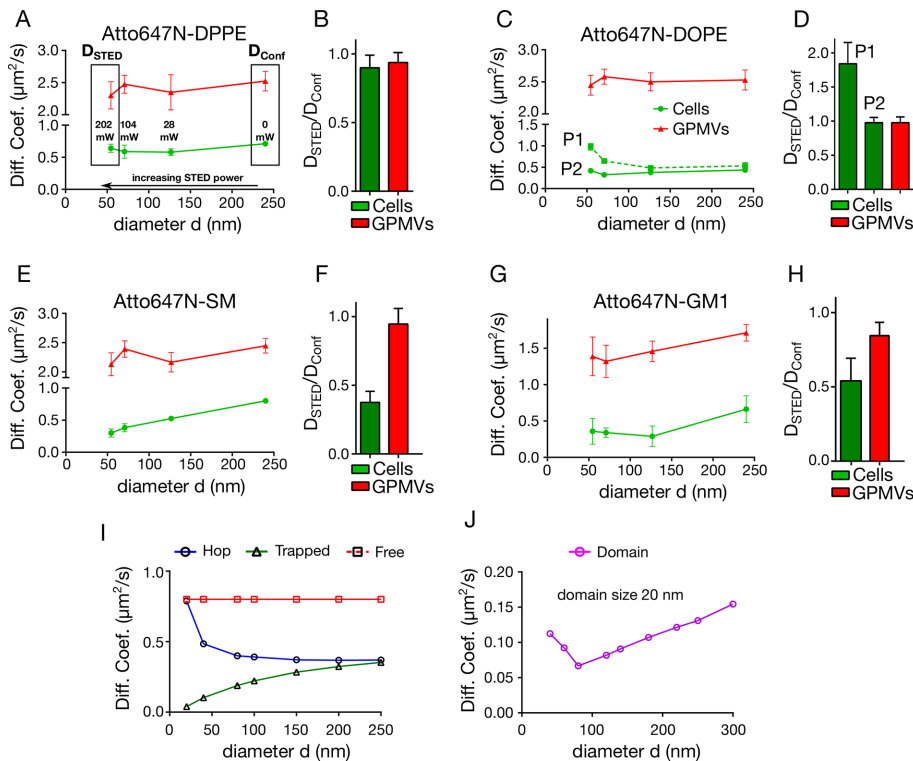


FIGURE 3: Diffusion modes of Atto647N-labeled lipid analogues in live cells (green) and GPMVs (red) revealed by STED-FCS. (A, C, E, G) Dependences of the apparent diffusion coefficient (D , Diff. Coef.) on the observation diameter (d) and (B, D, F, H) ratio $D_{\text{STED}}/D_{\text{Conf}}$ calculated from these $D(d)$ dependences (D_{STED} and D_{Conf} : diffusion coefficients at ~50- and 240-nm observation diameter, respectively) for (A, B) Atto647N-DPPE, (C, D) Atto647N-DOPE showing two different pools, P1 and P2, (E, F) Atto647N-SM, and (G, H) Atto647N-GM1. Error bars are SDs of the mean of at least 10 individual measurements on different cells or vesicles. D_{Conf} is the rightmost value in the graphs (STED laser power = 0), and D_{STED} is the leftmost (STED power \approx 200 mW). (I) Monte Carlo simulations of free (red), hop (blue), and trapped (green) diffusion, yielding the shown $D(d)$ dependences, as detailed in *Materials and Methods*. (J) Monte Carlo simulation of transient incorporation into 20-nm nanodomains. The resulting $D(d)$ dependence indicates a kink well above the domain size.

$D_{\text{STED}}/D_{\text{Conf}} \approx 0.38$ for Atto647N-SM (Figure 3F). In contrast, $D_{\text{STED}}/D_{\text{Conf}}$ values close to ~ 1 were found for all of these probes (except GM1, which will be discussed soon) in GPMVs, confirming their free diffusion in GPMV membrane. Diffusion of the lipid analogues in CHO cells confirmed that the observed diffusion modes were not specific to PtK2 cells (Supplemental Figure S7).

Actin-(in)dependent, transient nanodomain incorporation of GM1

In the case of Atto647N-GM1, we observed trapped-like diffusion in both live cells and GPMVs ($D_{\text{STED}}/D_{\text{Conf}} \approx 0.55$ in live cells and 0.83 in GPMVs; Figure 3, G and H) with approximately threefold difference in overall mobility, which was much lower than the approximately fivefold difference observed for the other lipid analogues. Therefore STED-FCS measurements confirmed the confocal FCS data (compare Figure 2E); hindered diffusion of GM1 is influenced by the actin cytoskeleton to a much smaller extent than that of sphingomyelin.

A closer look at the $D(d)$ dependence of Atto647N-GM1 in Figure 3G suggests that this lipid analogue may be transiently incorporated into nanodomains in both cells and GPMVs, unlike pure trapped diffusion observed for Atto647N-SM (compare also Figure 1, B and D). As mentioned, in purely trapped diffusion, a molecule

is not moving during the transient halt, whereas during domain incorporation, the “trapped” molecule is still diffusing with relatively slower velocity, causing a kink in the $D(d)$ plot (Figures 1D and 3G). This deviation from the linear decrease is small yet significant. Such transient domain incorporation of GM1 in artificial vesicles was previously suggested (Lozano *et al.*, 2013; Amaro *et al.*, 2016).

Simulations of diffusion modes

To confirm and better understand the observed phenomena, we carried out Monte Carlo simulations of different diffusion modes, namely free, hop, and trapped diffusion, as well as transient domain incorporation, and generated respective $D(d)$ dependences (see *Materials and Methods* for details). Obtained $D(d)$ dependences (Figure 3, I and J) were in accordance with those expected from theory (compare Figure 1) and with the experimental results. The $D_{\text{STED}}/D_{\text{Conf}}$ ratios from the simulated $D(d)$ dependences (with $d = 40$ nm for STED and 250 nm for confocal images) were comparable with those extracted from the experimental data (e.g., $D_{\text{STED}}/D_{\text{Conf}} \approx 1$ for free diffusion for Atto647N-DPPE; $D_{\text{STED}}/D_{\text{Conf}} \approx 0.3$ for trapped diffusion vs. ~ 0.3 – 0.4 for Atto647N-SM and ~ 1.3 – 1.8 for hop diffusion for Atto647N-DOPE). In addition, the general tendency of $D(d)$ dependence for transient incorporation into nanodomains as observed for GM1 was confirmed with simulations (Figure 3J). It is worth noting that the kink in the $D(d)$ plot appears at much larger observation spot diameters than the actual domain size.

Of course, the exact shape and positioning of the simulated $D(d)$ dependences depend on various parameters, such as diffusion coefficient of free movement between traps or within compartments, compartment sizes, hopping/trapping probabilities and times, and nanodomain sizes and inner-domain diffusion properties (Wawrezynieck *et al.*, 2005; Ruprecht *et al.*, 2011; Sachl *et al.*, 2016). Such parameters vary drastically from one cell to another, as well as within an individual cell (Vidomini *et al.*, 2015). A particular challenge for simulating the domain diffusion is the mobility of the domain itself (Sachl *et al.*, 2016). Moreover, individual molecules might go through different diffusion modes, such as trapped and hop diffusion simultaneously. Because this scenario may cause a kink as well if the incline (hop diffusion) and decline (trapped diffusion) in the $D(d)$ plot cancel each other, we simulated this situation. We found that trapped diffusion usually dominates the $D(d)$ dependence, with hop diffusion only leading to a general shift toward smaller values of D (Supplemental Figure S8). Consequently the most likely diffusion mode in the case of the GM1 analogue for both live cells and GPMVs is transient incorporation into relatively slowly moving nanodomains. Related to this, note that such GM1-containing nanodomains in GPMVs were apparent at 37°C and also in GPMVs prepared using NEM instead of PFA/DTT (Supplemental Figure S3).

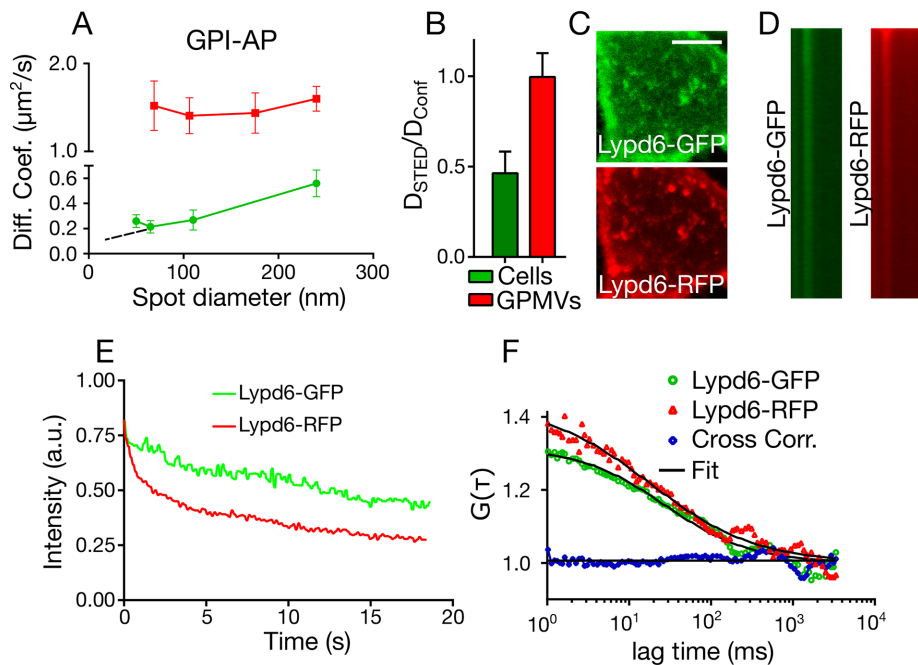


FIGURE 4: Diffusion of GPI-AP in cells and GPMVs. (A) Dependence of the apparent diffusion coefficient (D , Diff. Coef.) on the observation spot diameter (d) for GPI-SNAP in PtK2 cells (green, showing deviation from pure trapped diffusion, which is supposed to overlap with the dashed black line) and GPI-RFP labeled with a Atto647N-tagged nanobody in GPMVs (red), and (B) corresponding ratio $D_{\text{STED}}/D_{\text{Conf}}$ (with D_{STED} and D_{Conf} values of D at ~ 50 and 240 nm, respectively). Error bars are SDs of the mean of at least 10 measurements on different cells or vesicles. (C) Confocal images of cells expressing GPI-anchored Lypd6 proteins labeled with GFP (green; top) and RFP (red; bottom), showing overlapping bright clusters (Pearson $r = 0.51 \pm 0.1$). Scale bar, $10 \mu\text{m}$. (D, E) Fluorescence signal over time from the Lypd6 clusters for the GFP (green) and RFP (red) label. (D) Line scans (space, x-axis) vs. time (y-axis from top to bottom) with a bright signal spot fading over time, and (E) corresponding fluorescence intensity vs. time. (F) Autocorrelation (FCS; red and green) and cross-correlation (FCCS; blue) functions of Lypd6-GFP and Lypd6-RFP in the plasma membrane of live PtK2 cells, together with a fit to the data (black), showing high mobility of both Lypd6-GFP and Lypd6-RFP (FCS data) but no codiffusion (FCCS data). For FCCS controls, see Supplemental Figure S12.

Diffusion and organization of GPI-APs in cells and GPMVs

GPI-APs play important roles in multiple cellular processes, but their organization in the cell membrane is controversial (Sevcsik *et al.*, 2015). Thus we next investigated the diffusion and organization of GPI-APs in live cells and GPMVs. We expressed GPI-anchored SNAP-tag domains (GPI-SNAPs) in PtK2 and CHO cells and labeled them with the functionalized dye Abberior Star Red. STED microscopy images of the spatial organization of the GPI-APs in the live cells revealed ~ 100 -nm large, bright, and sparse clusters (Supplemental Figure S9A), which disappeared in the GPMVs. Further, confocal FCS data taken for GPI-SNAPs exhibited a much slower approximately fivefold diffusion in the live cells ($D \approx 0.5 \mu\text{m}^2/\text{s}$) compared with the GPMVs ($D \approx 2.5 \mu\text{m}^2/\text{s}$), similar to the Atto647N-DOPE lipid (Figure 2E). Finally, STED-FCS on GPI-SNAPs (Figure 4A) indicated trapped-like diffusion in live cells ($D_{\text{STED}}/D_{\text{Conf}} \approx 0.5$), which was abolished in GPMVs ($D_{\text{STED}}/D_{\text{Conf}} \approx 1$; Figure 4, A and B). For STED-FCS measurements of GPI-APs on GPMVs, we had to use a slightly modified labeling strategy because the GPI-SNAPs could not be labeled efficiently enough, yielding too low signal for the STED-FCS recordings. We therefore used red fluorescent protein (RFP)-tagged GPI-APs (GPI-RFP), whose fluorescence signal was further amplified using an Atto647N-labeled nanobody against RFP.

To exclude an influence by the SNAP-labeling strategy or by the choice of GPI-AP type, we also explored the dynamics and organiza-

tion of Lypd6. Lypd6 is a crucial GPI-AP involved in Wnt/ β -catenin signaling (Ozhan *et al.*, 2013). We expressed RFP-tagged Lypd6 proteins in PtK2 and CHO cells (Lypd6-RFP) and again further amplified their signal with an Atto647N-labeled nanobody against RFP. Lypd6-RFP also formed ~ 100 -nm large, bright, and sparse clusters (Supplemental Figure S9B) that were not visible in GPMVs (Supplemental Figure S10A) and revealed hindered, trapped-like diffusion in live cells but not in GPMVs ($D_{\text{STED}}/D_{\text{Conf}} \approx 0.4$ – 0.5 in live cells and ≈ 1 for GPMVs; Supplemental Figure S9C); similar to GPI-SNAP. We excluded possible artifacts due to unspecific binding of the nanobody to the coverslip surface, since we observed efficient and specific labeling of Lypd6-RFP on the membrane surface (Supplemental Figure S9D).

We sought to characterize further the ~ 100 -nm large, bright, and sparse clusters of the GPI-APs in live cells. First, we expressed GFP- and RFP-tagged Lypd6 (Lypd6-GFP and -RFP) proteins in PtK2 and CHO cells. Two-color confocal images confirmed the existence of bright and sparse clusters accommodating both Lypd6-GFP and Lypd6-RFP (Figure 4C; significant spatial overlap of GFP and RFP signals, Pearson $r = 0.51 \pm 0.1$). GFP- or RFP-tagged Lypd6 showed no visible signs of such bright and sparse clusters in GPMVs (Supplemental Figure S10A). Further, the clusters were immobile or extremely slowly moving (Supplemental Movie S1). Repetitive scanning over the visible clusters showed quickly fading fluorescence signals for both GFP and RFP (Figure 4, D and E), which shows that there was no fast interchange or replenishment of GPI-APs within these clusters. Finally, we confirmed that the clusters were plasma membrane entities and not endocytic vesicles by costaining with membrane- and endocytosis-specific markers (Supplemental Figure S11).

The static properties of these bright and sparse clusters revealed that they were not involved in the diffusion dynamics of the GPI-APs that we observed by the confocal and STED-FCS experiments. Consequently there must be two pools of GPI-APs in the live cells—one mobile pool and one organized in rather static clusters. Yet our STED-FCS measurements revealed that the diffusion of the mobile pool was still hindered. A close inspection of the $D(d)$ dependence of Figure 4A even indicates transient incorporation into nanodomains as for GM1 but with a dependence on the cortical actin, as this hindrance disappears in GPMVs. Comparison with our Monte Carlo simulations (Figure 3J) suggests that these nanodomains must be < 20 nm in diameter. We further studied transient trapping or nanodomain incorporation by fluorescence cross-correlation spectroscopy (FCCS) of Lypd6-GFP and Lypd6-RFP. We expected a non-zero FCCS curve amplitude in case of a significant codiffusion of GPI-APs, which would be the case for incorporation into stable and mobile nanodomains accommodating more than one GPI-AP. However, we observed near-zero amplitude in the FCCS curves between different Lypd6-GFP and Lypd6-RFP (Figure 4F). We confirmed this

using GPI-SNAP tagged with differently colored fluorophores, as well as GPI-GFP and GPI-RFP (Supplemental Figure S12). To validate the FCCS approach, we used control samples to test the alignment of our system, which could successfully identify codiffusing molecules (Supplemental Figure S12). It is worth noting that FCCS, due to noise issues, is probably not capable of revealing the codiffusion of a fairly small fraction (<5%) of codiffusing molecules (Kask *et al.*, 2000).

In conclusion, we identified two pools of GPI-APs in live cells—one organized in ~100-nm large, bright, sparse, and static clusters and another, highly mobile pool that transiently incorporates into <20-nm nanodomains. Both the static clusters and dynamic nanodomains were not detectable in the GPMVs, highlighting that both features were associated with the actin cytoskeleton. Note that the GPI-APs generally tend to partition into more ordered lipid environments (as probed in phase-separated GPMVs; Supplemental Figure S10B), highlighting that the clusters and/or nanodomains might be of high molecular order, thus exhibiting slower diffusion.

DISCUSSION

Using STED-FCS, we compared the diffusion modes of several fluorescent lipid analogues and GPI-APs in the plasma membrane of live cells and cell-derived GPMVs. In all cases, diffusion was much faster in GPMVs, and hindrances in diffusion were weakened or mostly abolished. Fluorescence imaging and FCS measurements of the cortical actin in cells compared with GPMVs demonstrated the absence of this network in GPMVs, suggesting the essential role of the actin cortex in maintaining hindered diffusion modes in living cells. Specifically, fluorescent DPPE, DOPE, and SM lipid analogues showed free, hop, and trapped diffusion in live PtK2 and CHO cells, respectively, and they all exhibited free diffusion with approximately fivefold increased diffusion coefficients in GPMVs. In contrast, the hindered diffusion of a fluorescent GM1 analogue in live cells was not completely abolished in GPMVs, with only a threefold increase in overall mobility. The STED-FCS data, supported by Monte Carlo simulations, suggested transient incorporation into nanodomains in both live cells and GPMVs. It seems that the actin cortex has much less influence on the diffusion dynamics of GM1 than, for example, of SM, confirming previous STED-FCS measurements using actin-perturbing drugs (Mueller *et al.*, 2011). The distinct diffusion characteristics of the GM1 might be crucial for its specific role in membrane bioactivity. GM1 is one of the most ubiquitous glycolipids of the cell membrane and is essential in host–pathogen interactions (Aureli *et al.*, 2016). Further, GM1 forms functional homodomains (Amaro *et al.*, 2016) or heterodomains with GPI-APs (Komura *et al.*, 2016).

For GPI-APs, we identified two pools in live cells—one organized in ~100-nm large, bright, sparse, and very static clusters, and another, highly mobile pool that transiently incorporates into nanodomains. Both the static clusters and dynamic nanodomains are not detectable in the GPMVs, suggesting that both features are associated with the actin cytoskeleton and that these nanodomains have a different nature than GM1 domains. The static clusters are most probably those highlighted in previous studies (Raghupathy *et al.*, 2015) and are completely separate from the mobile pool, in which we found no sign of codiffusing GPI-APs.

Our data confirm that hop diffusion can be explained by compartmentalization of the plasma membrane due to the underlying actin cytoskeleton (Fujiwara *et al.*, 2002; Andrade *et al.*, 2015). Moreover, the trapping of sphingomyelin is associated with the actin cytoskeleton, most probably due to interactions with molecules whose mobility is modulated by the actin cortex (Mueller *et al.*, 2011). However, in contrast to previous drug treatments (Mueller

et al., 2011; Andrade *et al.*, 2015), which may affect many other cellular features besides the actin cytoskeleton, here we investigated these dependences without the use of such drugs but instead on cell-derived plasma membranes. Although other factors, such as nonequilibrium processes (e.g., endocytosis and exocytosis) or membrane leaflet asymmetry are also believed to be absent in GPMVs (Sezgin *et al.*, 2012a), the absence of an intact actin cortex is the most prominent factor for influencing molecular membrane diffusion. Furthermore, the consensus of the differently designed experiments (drug treatments vs. GPMVs, or single-particle tracking vs. STED-FCS) manifests the strong role of the actin cytoskeleton in molecular membrane diffusion. Similarly, the strong dependence of the formation of sparse and static GPI-AP clusters on the actin cytoskeleton is also in accordance with previous biochemical and microscopy data (Sengupta *et al.*, 2011; Raghupathy *et al.*, 2015). Yet the simultaneous disclosure of another mobile pool of GPI-APs, which transiently incorporates into highly dynamic nanodomains, is novel, bringing a perspective to the possible controversies between the reported GPI-AP clusters and previous single-particle tracking studies (Wieser *et al.*, 2007; Pinaud *et al.*, 2009). Finally, although mild actin dependence of GM1-hindered diffusion has been reported before (Mueller *et al.*, 2011), more detailed analysis performed here highlights that this hindrance is due to the transient incorporation into nanodomains. It is intriguing that these domains are maintained without the actin cytoskeleton and in a passive environment of GPMVs. In general, dual-color STED-FCS will be required to further elucidate the diffusion modes, for example, by additionally labeling potential binding partners. A particularly interesting question is whether pronounced actin structures such as podosomes (van den Dries *et al.*, 2013) or stars, asters, and vortices (Kruse *et al.*, 2004; Fritzsche *et al.*, 2017) serve as pinning sites for interaction partners.

Another intriguing question is why the STED-FCS recordings of only certain molecules such as DOPE but not all molecules show hop diffusion. A reason could be the interplay between hop and trapped diffusion. Whereas hop diffusion leads to an increase in values of the apparent diffusion coefficient D with decreasing diameter of the observation spot, trapped diffusion shows the opposite effect. Our simulations show that the $D(d)$ dependence for a molecule undergoing both hop and trapped diffusion is usually dominated by the trapping, with the hopping leading only to a general shift toward smaller values of D . Most probably, all lipids encounter hop diffusion, yet trapping (or domain incorporation) is more pronounced for SM, GM1, and GPI-APs. Further, local variations in the actin organization or binding partners across the cell lead to different diffusion characteristics at different positions in the cells. This explains the presence of two distinct pools of diffusion for DOPE. Complementary methods such as high-speed single-particle tracking, camera-based FCS, or scanning STED-FCS, which can probe spatial heterogeneity in diffusion, will be able to resolve the remaining challenges while still requiring sufficient time resolution (Fujiwara *et al.*, 2002; Di Rienzo *et al.*, 2013; Honigsmann *et al.*, 2014; Spillane *et al.*, 2014; Moens *et al.*, 2015). More elaborate simulations of different diffusion modes may also give additional insight.

Lipid–lipid and lipid–protein interactions are believed to be important for plasma membrane organization and bioactivity (Sezgin *et al.*, 2017). Lipids have preferential interactions with other lipids and proteins due to their structural differences. For instance, sphingosine-based lipids can form hydrogen bonds with cholesterol (Ramstedt and Slotte, 1999), which is believed to be the basis for membrane raft domain formation, and several membrane proteins with binding pockets for specific lipids have been found (Contreras *et al.*, 2012).

These lipid–lipid or lipid–protein interactions obviously influence their diffusion characteristics, and thus understanding the principles behind heterogeneous diffusion modes will give important insight into cell membrane structure and dynamics and hence bioactivity. It is well accepted that lipid bulk properties influence the activity of signaling molecules (Wu *et al.*, 2016). Further, it has been shown that specific lipid–protein interactions modulate the activity of receptors (Coskun *et al.*, 2011; Laganowsky *et al.*, 2014). For these reasons, the organization of lipid species (particularly lipid-driven nanodomains) is of great importance. In a recent report, sphingomyelin metabolism was found to influence the dynamics of integrin clusters, proving a specific involvement of lipid dynamics in protein function (Eich *et al.*, 2016). In another example, GPI-AP nanoclusters were shown to influence integrin-dependent signaling (van Zanten *et al.*, 2009). Besides lipid-driven reorganization, cytoskeletal rearrangement was found to be a crucial player in signaling events (Mattila *et al.*, 2016). Thus an experimental system as presented here in which the diffusion of lipids and proteins with or without actin can be reliably measured is extremely valuable. The reach of our system is not limited to lipids and GPI-APs but can also be helpful for investigating the dependence of membrane receptor dynamics (e.g., clustering) on the actin cytoskeleton. Moreover, our methodology provides a straightforward system to distinguish energy-dependent active mechanisms (such as endocytosis and exocytosis) from energy-independent passive mechanisms. The hindered diffusion of GM1 in GPMVs we observed is an excellent example of such a passive event and of great interest because it has been shown that GM1 nanodomains are crucial for β -amyloid oligomerization, which plays an important role in Alzheimer disease (Amaro *et al.*, 2016). Our study confirms that this nanodomain formation of GM1 is not significantly dependent on the actin cytoskeleton or energy but instead is a passive clustering driven by presumably preferential interaction of lipids. In contrast, GPI-AP domain formation is strongly dependent on these factors, as they disappear in GPMVs. In conclusion, STED-FCS in combination with GPMVs serves as a powerful tool to reveal important details of molecular membrane organization and dynamics, particularly the role of organized cortical actin cytoskeleton.

MATERIALS AND METHODS

Tissue culture

PtK2 cells were grown in DMEM (Sigma-Aldrich) supplemented with 15% fetal bovine serum (FBS; Sigma-Aldrich) and 1% L-glutamine (Sigma-Aldrich). CHO cells were cultured in DMEM/F12 (Lonza) supplemented with 10% FBS and 1% L-glutamine. Jurkat T-cells were grown in RPMI 1640 (Sigma-Aldrich) containing 10% FBS, 1% L-glutamine, and 10 mM 4-(2-hydroxyethyl)-1-piperazineethanesulfonic acid (HEPES). RBL cells were cultured in DMEM (Sigma-Aldrich) supplemented with 10% FBS and 1% L-glutamine. For GPMV production, the cells were grown on 30 mm Petri dishes, and for diffusion measurements in live cells, they were grown on 18- or 25-mm round coverslips (#1.5). Usually, the cells reached a confluency of 50–70% before the measurement was performed.

Cell labeling

Cells were labeled in phenol red-free L15 medium (Sigma-Aldrich) at a lipid concentration of 1 μ g/ml (Atto647N-DPPE, -SM, -DOPE) for 15 min at room temperature. After two washes with L15, measurements were performed immediately. The labeling with Atto647N-H-GM1 was performed in full medium (2 μ g/ml) for 15 min at room temperature. Lipid analogues were not bovine serum albumin (BSA) coupled.

The lipid analogues Atto647N-DOPE, Atto647N-DPPE, and Atto647N-SM were purchased from Atto-Tec. Atto647N-GM1 (C18:1, C18:0) was synthesized by Guenter Schwartzmann (University of Bonn, Bonn, Germany; Eggeling *et al.*, 2009). TF-Chol was purchased from Avanti Polar Lipids. Transfections for PtK2 cells were performed using Lipofectamine 3000 (Thermo Fisher), and transfections for CHO cells were performed using Turbofect (Thermo Fisher), according to the manufacturer's protocols. See Ozhan *et al.* (2013) for Lypd6-GFP and Lypd-RFP. GPI-SNAP was a gift from the lab of Stefan Hell (Max Planck Institute for Biophysical Chemistry, Göttingen, Germany), VAMP7 was obtained from the Wolfson Imaging Centre (Oxford, United Kingdom), and GPI-GFP and GPI-RFP were obtained from the lab of Kai Simons (Max Planck Institute of Molecular Cell Biology and Genetics, Dresden, Germany).

Labeling of GPI-RFP or Lypd6-RFP was performed with an RFP-binding nanobody labeled with Atto647N (ChromoTek). The nanobody was diluted to 100 μ g/ml in 4% BSA in phosphate-buffered saline (PBS) and stored at 4°C. Labeling was performed at a final concentration of 1 μ g/ml.

SNAP labeling with Abberior Star Red (Abberior) was performed at 2 μ g/ml in full medium at 37°C for 30 min. After two washing steps with full medium at 37°C (30 min each), STED-FCS measurements and imaging were performed in L15.

Cell-mask labeling was done by adding 0.5 μ M (final concentration) CellMask Deep Red (Thermo Fisher) in full medium. It was incubated for 15 min at room temperature and washed twice with L15 afterward.

GPMVs

Cell-derived GPMVs were prepared according to Sezgin *et al.* (2012a). Briefly, cells were grown to a confluency of ~70%, washed with GPMV buffer (containing 10 mM HEPES, 150 mM NaCl, 2 mM CaCl_2 , pH 7.4), and after adding 2 mM DTT and 25 mM PFA, the cells were incubated for at least 4 h (PtK2 cells) or 2 h (CHO/RBL cells) at 37°C to allow the cells to produce a sufficient amount of GPMVs. In the case of the vesiculation agent NEM, the cells were washed with GPMV buffer and incubated with 2 mM NEM in GPMV buffer for not longer than 2 h. GPMVs from T-cells were prepared using NEM as previously described (Koller *et al.*, 2017).

Labeling and immobilization of GPMVs

The GPMV-containing supernatant was harvested. DSPE-PEG-biotin (Avanti Polar Lipids) was added to a final concentration of 0.2 μ g/ml into the GPMV suspension. After 1.5 h, GPMVs were labeled with the ethanol-dissolved lipid analogue Atto647N-DPPE, Atto647N-SM, or Atto647N-DOPE. They were added to the GPMV solution to a final concentration of 0.1, 0.2, and 0.14 μ g/ml, respectively. Atto647N-GM1 was dissolved in dimethyl sulfoxide and was added to a final concentration of 4 μ g/ml. After another 15 min of incubation, the GPMVs were spun down at 10,000 rpm for 15 min, and the supernatant was replaced by fresh buffer. The last step was crucial for the removal of free biotinylated lipid. For the measurements of GPI-RFP or Lypd6-RFP, an RFP-binding nanobody labeled with Atto647N was added to a final concentration of 2 μ g/ml before spinning the GPMVs down.

The GPMVs were immobilized using biotin and streptavidin. Glass coverslips were coated with a 5:1 mixture of BSA/biotinylated BSA (Sigma-Aldrich) for 1.5 h, extensively washed, and incubated with a solution of 200 ng/ml streptavidin (Life Technologies) in PBS. After washing with GPMV buffer, the biotinylated GPMVs were added. Measurements were performed after 20 min. Immobilized GPMVs were stable for several hours.

The formation of GPMVs from other cell lines (CHO or Jurkat) was much faster than for PtK2 (within 2 h). Otherwise, these GPMVs were formed and treated in the same way. The GPMVs were tested for the phase separation before to ensure that they were not phase separated at room temperature. GPMVs from PtK2 cells were found to phase separate below 10°C, and thus they were not phase separated at room temperature (Supplemental Figure S4). Fast-DiO (Sigma Aldrich) and Abberior Star Red-PEG-DSPE were added to GPMV with 100 ng/ml final concentration to label disordered and ordered phases, respectively.

GUVs

GUVs were prepared by electroformation (Garcia-Saez *et al.*, 2010). A solution of DOPC (Avanti Polar Lipids) with a concentration of 1 mg/ml in chloroform was spread on platinum wires. After solvent evaporation, the electrodes were dipped into 300 mM sucrose. An electric field with a frequency of 10 Hz and a potential of 2 V was applied for 1 h, followed by a frequency of 2 Hz. GUVs were handled with cut tips and measurements performed in PBS. Coverslips were coated with BSA. GUVs were labeled by adding the lipid analogues TopFluor-Cholesterol (Avanti Polar Lipids), Atto47N-DOPE, Atto647N-SM, or Atto647N-DPPE to a final concentration of 0.05 µg/ml. Atto647N-GM1 was used at a final concentration of 0.005 µg/ml.

Supported lipid bilayers

Supported lipid bilayers were prepared by spin coating (Clausen *et al.*, 2015). The coverslips were previously cleaned and edged by piranha acid (3:1 sulfuric acid and hydrogen peroxide). Coverslips were stored in water for not longer than 1 wk.

A solution of 1 mg/mL DOPC in chloroform/methanol was spin coated onto a coverslip at 3200 rpm for 45 s. The lipid bilayer formed by rehydration with SLB buffer containing 10 mM HEPES and 150 mM NaCl pH 7.4. The SLB was labeled with AbberiorStar Red-DPPE (~1:2000 M ratio; Abberior) contained in the initial DOPC solution.

Data acquisition and evaluation

Confocal imaging, confocal FCS, and FCCS measurements were taken on a Zeiss780 LSM inverted confocal microscope equipped with a 40× C-Apochromat NA 1.2 W Corr FCS objective (Zeiss). We used labeled high-density lipoprotein particles (a gift from Herbert Stangl, MedUni Wien, Vienna, Austria) as FCCS positive control and a mixture of Alexa 488 and Alexa 647 as negative control to ensure that the microscope was aligned and full cross-correlation could be obtained. Aside from the control of Atto647N-GM1 in GPMVs (37°C), all measurements were performed at room temperature.

All STED-FCS and STED imaging data were taken on a custom-built Abberior STED microscope (Abberior Instruments) as previously described (Clausen *et al.*, 2014; Galiani *et al.*, 2016). The microscope was equipped with a hardware correlator (Flex02-08D, operated by the manufacturer's software; Correlator.com). The dyes were excited using a 640-nm pulsed diode laser (80-MHz repetition rate; PicoQuant) with an average excitation power of 5–10 µW at the objective (UPlanSApo 100×/1.4 oil; Olympus). For STED recordings, fluorescence emission was inhibited using a Mai Tai tunable pulsed laser at 780 nm (80-MHz repetition rate; Newport) with a donut-shaped focal intensity pattern formed by a phase plate within the beam path. The microscope was operated using Abberior's Imspector software.

Using the FoCuS-point fitting software (Waithe *et al.*, 2016), all FCS data on membrane diffusion in SLBs, GUVs, and GPMVs were

fitted to a two-dimensional (2D) diffusion model including triplet-state kinetics (with a fixed relaxation time of 5 µs). For measurements in the plasma membrane of living cells, additional dark-state kinetics (with a fixed relaxation time of 100 µs) for the data of all Atto647N-labeled lipids had to be assumed (as pointed out in Mueller *et al.*, 2013). The data on free cytoplasmic GFP and Lifeact-GFP were fitted using a three-dimensional diffusion equation with one or two components after determination of the structural parameter by measurements of Alexa 488 in water.

In the STED-FCS measurements, the diameter, d , of the observation spot is tuned by the average power P_{STED} of the STED laser. We performed STED-FCS measurements of AbberiorStar Red-DPPE in SLBs and GUVs at different P_{STED} to accurately calibrate the $d(P_{\text{STED}})$ dependence; more specifically we performed these calibration measurements before every experiments on SLBs (100% DOPC) for the STED-FCS recordings on living cells and on GUVs (100% DOPC) for those on GPMVs. Because AbberiorStar Red-DPPE diffuses freely in both model membranes, we can calculate the $d(P_{\text{STED}})$ dependence using the following equation:

$$d = 240 \text{ nm} \cdot \sqrt{(\tau_{D(\text{STED})} / \tau_{D(\text{conf})})}$$

$\tau_{D(\text{conf})}$ and $\tau_{D(\text{STED})}$ are the transit times of the investigated molecules through the observation spot in confocal and at a certain STED laser power, respectively. The confocal observation spot diameter of $d = 240$ nm was determined from confocal images of 20-nm Crimson beads (Life Technologies) spread out on a poly-L-lysine (Sigma Aldrich)-coated glass coverslip.

The (apparent) diffusion coefficient, D , was calculated from $\tau_{D(\text{conf})}$ and $\tau_{D(\text{STED})}$ according to

$$D = \frac{d^2}{8 \cdot \ln(2) \cdot \tau_D}$$

At least 5–10 different cells were measured for each probe within a single measurement session, resulting in multiple FCS measurements (5–15 s) at different spots across the cell for every STED power. All measurements were repeated at least three times to confirm the reproducibility. Each single set of measurement was carried out in the same region of the cell at different spot sizes (STED laser powers). Power gradient was applied in the reverse order as well to avoid any artifacts due to the increasing laser power (confocal to high STED power and vice versa). Each data point in the graphs show the average of the different days and different cells. Error bars are the SDs of the mean.

Simulations

We performed Monte Carlo simulations to generate molecular tracks that characterized the different diffusion modes in our investigation. We generated fluorescence traces by passing the generated tracks through Gaussian spots of varying diameter, representative of the effect that different STED powers would have on the detection volume. Simulations were performed in a 2D circular space of radius 2500 nm and iterated using a 0.02-ms time step for a 20-s total duration. One hundred molecules were randomly initiated within the simulation, each with a free diffusion rate of 0.8 µm²/s. Molecules that diffused across the simulation boundary were wrapped to the opposite edge of the simulation boundary.

Trap diffusion in the first instance was simulated using a stochastic trapping model in which free diffusion is hindered randomly by molecular complex formation (Ringemann *et al.*, 2009). In this mode, at each time step, we evaluate a probability for switching from the

free diffusion state to the hindered state ($D = 0.1 \times 10^{-9} \mu\text{m}^2/\text{s}$) and vice versa (in this case, with a probability of $p = 0.002$ in both directions) corresponding to rates $k_{\text{on}} = k_{\text{off}} = 8 \times 10^5$ for binding and release. For the simulation of hop diffusion, we first generated a mesh by randomly dispersing points on a grid and then applying a Voronoi transform on these points. Enough points were added to yield an average Voronoi region size of 100 nm in diameter (diameter calculated as $\sqrt{\text{area}}$). Molecules in the hop diffusion simulation that randomly walked into new regions were only allowed to pass into that region based on probability $p_{\text{hop}} = 0.25$. If, upon evaluation, the molecule failed p_{hop} , it would move randomly in its existing region for that time step, whereas otherwise it would transition into the new region.

The spatial domain trapping simulation—an alternative to trapping through molecular complex formation—was performed by distributing circular domains of diameter 20 nm across the simulation area. Enough domains were distributed to cover 50% of the simulation space, and the positions were randomly perturbed over many iterations to ensure that the distribution of domains was random. Furthermore, during the random perturbation process, the domains were prevented from overlapping through a hard constraint. During the simulation, particles that crossed into or out of the domains would only be allowed to do so after evaluation of a probability test with a probability less than the p_{hop} value ($p = 0.002$), corresponding to the same rate constant as in the stochastic trapping model. During the simulation, particles that crossed into or out of the domains would only do so if, upon evaluation of a probability, the test was less than the p_{hop} value ($p = 0.002$), corresponding to the same rate constant as in the stochastic trapping model. Diffusion inside the circular domains was reduced to $D_{\text{in}} = D/3.0$, one-third of $0.8 \mu\text{m}^2/\text{s}$.

For each simulation, 10 random locations for focal spots were chosen, and in each location, nine different focal spots sizes (40–300 nm) were applied; each simulation was repeated five times, generating 50 replicates for each focal spot size. Intensity traces were correlated using a multiple-tau correlation algorithm (Wahl *et al.*, 2003) and fitted using the foregoing procedure.

ACKNOWLEDGMENTS

We thank Christoffer Lagerholm and Esther Garcia for help on the microscopes in the Wolfson Imaging Centre. E.S. is supported by EMBO long-term (ALTF 636-2013) and Marie Skłodowska-Curie Intra-European Fellowships (MEMBRANE DYNAMICS-627088). This work was supported by the Wolfson Foundation (Grant 18272), the Medical Research Council (Grant MC_UU_12010/Unit Programmes G0902418 and MC_UU_12025), MRC/BBSRC/ESPRC (Grant MR/K01577X/1), the Wellcome Trust (Grants 107457/Z/15/Z and 104924/14/Z/14), Oxford-internal grants (John-Fell Fund and EPA Cephalosporin Fund), the Scientific and Technological Research Council of Turkey (Grant 114Z192), an EMBO Installation Grant to G.O. (Grant 3024), and the Newton-Katip Celebi Fund.

REFERENCES

Amaro M, Sachl R, Aydogan G, Mikhalyov II, Vacha R Hof M (2016). GM1 ganglioside inhibits beta-amyloid oligomerization induced by sphingomyelin. *Angew Chem Int Ed Engl* 55, 9411–9415.

Andrade DM, Clausen MP, Keller J, Mueller V, Wu C, Bear JE, Hell SW, Lagerholm BC, Eggeling C (2015). Cortical actin networks induce spatiotemporal confinement of phospholipids in the plasma membrane—a minimally invasive investigation by STED-FCS. *Sci Rep* 5, 11454.

Aureli M, Mauri L, Ciampa MG, Prinetti A, Toffano G, Secchieri C, Sonnino S (2016). GM1 ganglioside: past studies and future potential. *Mol Neurobiol* 53, 1824–1842.

Baumgart T, Hammond AT, Sengupta P, Hess ST, Holowka DA, Baird BA, Webb WW (2007). Large-scale fluid/fluid phase separation of proteins and lipids in giant plasma membrane vesicles. *Proc Natl Acad Sci USA* 104, 3165–3170.

Blouin CM, Hamon Y, Gonnord P, Boularan C, Kagan J, Viaris de Lesegno C, Ruez R, Mailfert S, Bertaux N, Loew D, *et al.* (2016). Glycosylation-dependent IFN-gammaR partitioning in lipid and actin nanodomains is critical for JAK activation. *Cell* 166, 920–934.

Chinnapen DJ, Hsieh WT, te Welscher YM, Saslowsky DE, Kaoutzani L, Brandsma E, D'Auria L, Park H, Wagner JS, Drake KR, *et al.* (2012). Lipid sorting by ceramide structure from plasma membrane to ER for the cholera toxin receptor ganglioside GM1. *Dev Cell* 23, 573–586.

Clausen MP, Colin-York H, Schneider F, Eggeling C, Fritzsche M (2017). Dissecting the actin cortex density and membrane-cortex distance in living cells by super-resolution microscopy. *J Phys D Appl Phys* 50, 064002.

Clausen MP, Galiani S, De La Serna JB, Fritzsche M, Chojnacki J, Gehmlich K, Lagerholm BC, Eggeling C (2014). Pathways to optical STED microscopy. *NanoBiolmaging* 1, 1–12.

Clausen MP, Lagerholm BC (2013). Visualization of plasma membrane compartmentalization by high-speed quantum dot tracking. *Nano Lett* 13, 2332–2337.

Clausen MP, Sezgin E, Bernardino de la Serna J, Waithe D, Lagerholm BC, Eggeling C (2015). A straightforward approach for gated STED-FCS to investigate lipid membrane dynamics. *Methods* 88, 67–75.

Contreras FX, Ernst AM, Haberkant P, Bjorkholm P, Lindahl E, Gonen B, Tischer C, Elofsson A, von Heijne G, Thiele C, *et al.* (2012). Molecular recognition of a single sphingolipid species by a protein's transmembrane domain. *Nature* 481, 525–529.

Coskun U, Grzybek M, Drechsel D, Simons K (2011). Regulation of human EGF receptor by lipids. *Proc Natl Acad Sci USA* 108, 9044–9048.

Di Rienzo C, Gratton E, Beltram F, Cardarelli F (2013). Fast spatiotemporal correlation spectroscopy to determine protein lateral diffusion laws in live cell membranes. *Proc Natl Acad Sci USA* 110, 12307–12312.

Dustin ML, Groves JT (2012). Receptor signaling clusters in the immune synapse. *Annu Rev Biophys* 41, 543–556.

Eggeling C (2015). Super-resolution optical microscopy of lipid plasma membrane dynamics. *Essays Biochem* 57, 69–80.

Eggeling C, Ringemann C, Medda R, Schwarzmann G, Sandhoff K, Polyakova S, Belov VN, Hein B, von Middendorff C, Schönl A, Hell SW (2009). Direct observation of the nanoscale dynamics of membrane lipids in a living cell. *Nature* 457, 1159–1162.

Eich C, Manzo C, de Keijzer S, Bakker GJ, Reinieren-Beeren I, Garcia-Parajo MF, Cambi A (2016). Changes in membrane sphingolipid composition modulate dynamics and adhesion of integrin nanoclusters. *Sci Rep* 6, 20693.

Fahey PF, Koppel DE, Barak LS, Wolf DE, Elson EL, Webb WW (1977). Lateral diffusion in planar lipid bilayers. *Science* 195, 305–306.

Fritzsche M, Li D, Colin-York H, Chang V, Moendardary E, Felce J, Sezgin E, Charras G, Betzig E, Eggeling C (2017). Self-organizing actin patterns shape membrane architecture but not cell mechanics. *Nat Commun* 8, 14347.

Fujiwara T, Ritchie K, Murakoshi H, Jacobson K, Kusumi A (2002). Phospholipids undergo hop diffusion in compartmentalized cell membrane. *J Cell Biol* 157, 1071–1081.

Fujiwara TK, Iwasawa K, Kalay Z, Tsunoyama TA, Watanabe Y, Umemura YM, Murakoshi H, Suzuki KG, Nemoto YL, Morone N, Kusumi A (2016). Confined diffusion of transmembrane proteins and lipids induced by the same actin meshwork lining the plasma membrane. *Mol Biol Cell* 27, 1101–1119.

Galiani S, Waithe D, Reglinski K, Cruz-Zaragoza LD, Garcia E, Clausen MP, Schliebs W, Erdmann R, Eggeling C (2016). Super resolution microscopy reveals compartmentalization of peroxisomal membrane proteins. *J Biol Chem* 291, 16948–16962.

Garcia-Saez AJ, Carrer DC, Schwillie P (2010). Fluorescence correlation spectroscopy for the study of membrane dynamics and organization in giant unilamellar vesicles. *Methods Mol Biol* 606, 493–508.

Guymarc'h F, Zou S, Chen M, Milhiet P-E, Godefroy C, Vie V, Lopez C (2014). Milk sphingomyelin domains in biomimetic membranes and the role of cholesterol: morphology and nanomechanical properties investigated using AFM and force spectroscopy. *Langmuir* 30, 6516–6524.

Guzman C, Solman M, Ligabue A, Blazevits O, Andrade DM, Raymond L, Eggeling C, Abankwa D (2014). The efficacy of Raf kinase recruitment to the GTPase H-ras depends on H-ras membrane conformer-specific nanoclustering. *J Biol Chem* 289, 9519–9533.

- He HT, Marguet D (2011). Detecting nanodomains in living cell membrane by fluorescence correlation spectroscopy. *Annu Rev Phys Chem* 62, 417–436.
- Hiramoto-Yamaki N, Tanaka KAK, Suzuki KGN, Hirose KM, Miyahara MSH, Kalay Z, Tanaka K, Kasai RS, Kusumi A, Fujiwara TK (2014). Ultra-fast diffusion of a fluorescent cholesterol analog in compartmentalized plasma membranes. *Traffic* 15, 583–612.
- Honigsmann A, Mueller V, Hell SW, Eggeling C (2013). STED microscopy detects and quantifies liquid phase separation in lipid membranes using a new far-red emitting fluorescent phosphoglycerolipid analogue. *Faraday Discuss* 161, 77–89.
- Honigsmann A, Mueller V, Ta H, Schoenle A, Sezgin E, Hell SW, Eggeling C (2014). Scanning STED-FCS reveals spatiotemporal heterogeneity of lipid interaction in the plasma membrane of living cells. *Nat Commun* 5, 5412–5412.
- Houser JR, Busch DJ, Bell DR, Li B, Ren P, Stachowiak JC (2016). The impact of physiological crowding on the diffusivity of membrane bound proteins. *Soft Matter* 12, 2127–2134.
- Kahya N, Scherfeld D, Bacia K, Poolman B, Schwille P (2003). Probing lipid mobility of raft-exhibiting model membranes by fluorescence correlation spectroscopy. *J Biol Chem* 278, 28109–28115.
- Kask P, Palo K, Fay N, Brand L, Mets U, Ullmann D, Jungmann J, Pschorr J, Gall K (2000). Two-dimensional fluorescence intensity distribution analysis: theory and applications. *Biophys J* 78, 1703–1713.
- Klotzsch E, Schuetz GJ (2013). A critical survey of methods to detect plasma membrane rafts. *Philos Trans R Soc Lond B Biol Sci* 368, 20120033.
- Koller T, Blok S, Santos AM, Oszmiana A, Davis DM, Sezgin E, Eggeling C (2017). Rituximab capping triggers intracellular reorganization of B cells. *Matters* 2017(Jan 12), 10.19185/matters.201612000001.
- Komura N, Suzuki KG, Ando H, Konishi M, Koikeda M, Imamura A, Chadda R, Fujiwara TK, Tsuboi H, Sheng R, Cho W, et al. (2016). Raft-based interactions of gangliosides with a GPI-anchored receptor. *Nat Chem Biol* 12, 402–410.
- Koster DV, Husain K, Iljazi E, Bhat A, Bieling P, Mullins RD, Rao M, Mayor S (2016). Actomyosin dynamics drive local membrane component organization in an in vitro active composite layer. *Proc Natl Acad Sci USA* 113, E1645–E1654.
- Koster DV, Mayor S (2016). Cortical actin and the plasma membrane: inextricably intertwined. *Curr Opin Cell Biol* 38, 81–89.
- Kruse K, Joanny JF, Julicher F, Prost J, Sekimoto K (2004). Asters, vortices, and rotating spirals in active gels of polar filaments. *Phys Rev Lett* 92, 078101.
- Kusumi A, Nakada C, Ritchie K, Murase K, Suzuki K, Murakoshi H, Kasai RS, Kondo J, Fujiwara T (2005). Paradigm shift of the plasma membrane concept from the two-dimensional continuum fluid to the partitioned fluid: High-speed single-molecule tracking of membrane molecules. *Annu Rev Biophys Biomol Struct* 34, 351–354.
- Kusumi A, Shirai YM, Koyama-Honda I, Suzuki KGN, Fujiwara TK (2010). Hierarchical organization of the plasma membrane: investigations by single-molecule tracking vs. fluorescence correlation spectroscopy. *FEBS Lett* 584, 1814–1823.
- Laganowsky A, Reading E, Allison TM, Ulmschneider MB, Degiacomi MT, Baldwin AJ, Robinson CV (2014). Membrane proteins bind lipids selectively to modulate their structure and function. *Nature* 510, 172–175.
- Lingwood D, Simons K (2010). Lipid rafts as a membrane-organizing principle. *Science* 327, 46–50.
- Lozano MM, Liu Z, Sunnick E, Janshoff A, Kumar K, Boxer SG (2013). Colocalization of the ganglioside GM1 and cholesterol detected by secondary ion mass spectrometry. *J Am Chem Soc* 135, 5620–5630.
- Mattila PK, Batista FD, Treanor B (2016). Dynamics of the actin cytoskeleton mediates receptor cross talk: an emerging concept in tuning receptor signaling. *J Cell Biol* 212, 267–280.
- Moens PD, Digman MA, Gratton E (2015). Modes of diffusion of cholera toxin bound to GM1 on live cell membrane by image mean square displacement analysis. *Biophys J* 108, 1448–1458.
- Mueller V, Honigsmann A, Ringemann C, Medda R, Schwarzmann G, Eggeling C (2013). FCS in STED microscopy: studying the nanoscale of lipid membrane dynamics. *Methods Enzymol* 519, 1–38.
- Mueller V, Ringemann C, Honigsmann A, Schwarzmann G, Medda R, Leutenegger M, Polyakova S, Belov VN, Hell SW, Eggeling C (2011). STED microscopy reveals molecular details of cholesterol- and cytoskeleton-modulated lipid interactions in living cells. *Biophys J* 101, 1651–1660.
- Ozhan G, Sezgin E, Wehner D, Pfister AS, Kuehl SJ, Kagermeier-Schenk B, Kuehl M, Schwille P, Weidinger G (2013). Lypd6 enhances Wnt/beta-catenin signaling by promoting Lrp6 phosphorylation in raft plasma membrane domains. *Dev Cell* 26, 331–345.
- Pike LJ (2006). Rafts defined: a report on the Keystone Symposium on Lipid Rafts and Cell Function. *J Lipid Res* 47, 1597–1598.
- Pinaud F, Michalet X, Iyer G, Margeat E, Moore H-P, Weiss S (2009). Dynamic partitioning of a glycosyl-phosphatidylinositol-anchored protein in glycosphingolipid-rich microdomains imaged by single-quantum dot tracking. *Traffic* 10, 691–712.
- Polley A, Orlovski A, Danne R, Gurtovenko AA, Bernardino de la Serna J, Eggeling C, Davis SJ, Rog T, Vattulainen I (2017). Glycosylation and lipids working in concert direct CD2 ectodomain orientation and presentation. *J Phys Chem Lett* 1060–1066.
- Raghupathy R, Anilkumar AA, Polley A, Singh PP, Yadav M, Johnson C, Suryawanshi S, Saikam V, Sawant SD, Panda A, et al. (2015). Transbilayer lipid interactions mediate nanoclustering of lipid-anchored proteins. *Cell* 161, 581–594.
- Ramstedt B, Slotte JP (1999). Interaction of cholesterol with sphingomyelins and acyl-chain-matched phosphatidylcholines: a comparative study of the effect of the chain length. *Biophys J* 76, 908–915.
- Ringemann C, Harke B, Middendorff CV, Medda R, Honigsmann A, Wagner R, Leutenegger M, Schoenle A, Hell S, Eggeling C (2009). Exploring single-molecule dynamics with fluorescence nanoscopy. *New J Phys* 11, 103054.
- Ritchie K, Iino R, Fujiwara T, Murase K, Kusumi A (2003). The fence and picket structure of the plasma membrane of live cells as revealed by single molecule techniques (Review). *Mol Membr Biol* 20, 13–18.
- Ruprecht V, Wieser S, Marguet D, Schutz GJ (2011). Spot variation fluorescence correlation spectroscopy allows for superresolution chronoscopy of confinement times in membranes. *Biophys J* 100, 2839–2845.
- Sachl R, Bergstrand J, Widengren J, Hof M (2016). Fluorescence correlation spectroscopy diffusion laws in the presence of moving nanodomains. *J Phys D Appl Phys* 49, 114002.
- Saha S, Anilkumar AA, Mayor S (2016). GPI-anchored protein organization and dynamics at the cell surface. *J Lipid Res* 57, 159–175.
- Saka SK, Honigsmann A, Eggeling C, Hell SW, Lang T, Rizzoli SO (2014). Multi-protein assemblies underlie the mesoscale organization of the plasma membrane. *Nat Commun* 5, 4509.
- Schwarzer R, Levental I, Gramatica A, Scolari S, Buschmann V, Veit M, Herrmann A (2014). The cholesterol-binding motif of the HIV-1 glycoprotein gp41 regulates lateral sorting and oligomerization. *Cell Microbiol* 16, 1565–1581.
- Schwille P, Korlach J, Webb WW (1999). Fluorescence correlation spectroscopy with single-molecule sensitivity on cell and model membranes. *Cytometry* 36, 176–182.
- Scott RE, Maercklein PB (1979). Plasma membrane vesiculation in 3T3 and SV3T3 cells. II. Factors affecting the process of vesiculation. *J Cell Sci* 35, 245–252.
- Sengupta P, Jovanovic-Talisman T, Skoko D, Renz M, Veatch SL, Lippincott-Schwartz J (2011). Probing protein heterogeneity in the plasma membrane using PALM and pair correlation analysis. *Nat Methods* 8, 969–975.
- Sevcsik E, Brameshuber M, Folser M, Weghuber J, Honigsmann A, Schutz GJ (2015). GPI-anchored proteins do not reside in ordered domains in the live cell plasma membrane. *Nat Commun* 6, 6969.
- Sezgin E, Davis SJ, Eggeling C (2015a). Membrane nanoclusters-tails of the unexpected. *Cell* 161, 433–434.
- Sezgin E, Gutmann T, Buhl T, Dirx R, Grzybek M, Coskun U, Solimena M, Simons K, Levental I, Schwille P (2015b). Adaptive lipid packing and bioactivity in membrane domains. *PLoS One* 10, e0123930.
- Sezgin E, Kaiser H-J, Baumgart T, Schwille P, Simons K, Levental I (2012a). Elucidating membrane structure and protein behavior using giant plasma membrane vesicles. *Nat Protocols* 7, 1042–1051.
- Sezgin E, Levental I, Grzybek M, Schwarzmann G, Mueller V, Honigsmann A, Belov VN, Eggeling C, Coskun U, Simons K, Schwille P (2012b). Partitioning, diffusion, and ligand binding of raft lipid analogs in model and cellular plasma membranes. *Biochim Biophys Acta* 1818, 1777–1784.
- Sezgin E, Levental I, Mayor S, Eggeling C (2017). The mystery of membrane organization: composition, regulation and physiological relevance of lipid rafts. *Nat Rev Mol Cell Biol*, 10.1038/nrm.2017.16.
- Sezgin E, Schwille P (2012). Model membrane platforms to study protein-membrane interactions. *Mol Membr Biol* 29, 144–154.
- Simons K, Gerl MJ (2010). Revitalizing membrane rafts: new tools and insights. *Nat Rev Mol Cell Biol* 11, 688–699.
- Simons K, Ikonen E (1997). Functional rafts in cell membranes. *Nature* 387, 569–572.
- Singer SJ, Nicolson GL (1972). The fluid mosaic model of the structure of cell membranes. *Science* 175, 720–731.

- Solanko LM, Honigsmann A, Midtby HS, Lund FW, Brewer JR, Dekaris V, Bittman R, Eggeling C, Wustner D (2013). Membrane orientation and lateral diffusion of BODIPY-cholesterol as a function of probe structure. *Biophys J* 105, 2082–2092.
- Spillane KM, Ortega-Arroyo J, de Wit G, Eggeling C, Ewers H, Wallace MI, Kukura P (2014). High-speed single-particle tracking of GM1 in model membranes reveals anomalous diffusion due to interleaflet coupling and molecular pinning. *Nano Lett* 14, 5390–5397.
- van den Dries K, Schwartz SL, Byars J, Meddens MBM, Bolomini-Vittori M, Lidke DS, Figdor CG, Lidke KA, Cambi A (2013). Dual-color superresolution microscopy reveals nanoscale organization of mechanosensory podosomes. *Mol Biol Cell* 24, 2112–2123.
- van Zanten TS, Cambi A, Koopman M, Joosten B, Figdor CG, Garcia-Parajo MF (2009). Hotspots of GPI-anchored proteins and integrin nanoclusters function as nucleation sites for cell adhesion. *Proc Natl Acad Sci USA* 106, 18557–18562.
- Varma R, Mayor S (1998). GPI-anchored proteins are organized in submicron domains at the cell surface. *Nature* 394, 798–801.
- Vicidomini G, Ta H, Honigsmann A, Mueller V, Clausen MP, Waithe D, Galiani S, Sezgin E, Diaspro A, Hell SW, Eggeling C (2015). STED-FLCS: an advanced tool to reveal spatiotemporal heterogeneity of molecular membrane dynamics. *Nano Lett* 15, 5912–5918.
- Wahl M, Gregor I, Patting M, Enderlein J (2003). Fast calculation of fluorescence correlation data with asynchronous time-correlated single-photon counting. *Opt Express* 11, 3583–3591.
- Waithe D, Clausen MP, Sezgin E, Eggeling C (2016). FoCuS-point: software for STED fluorescence correlation and time-gated single photon counting. *Bioinformatics* 32, 958–960.
- Wawrezinieck L, Rigneault H, Marguet D, Lenne PF (2005). Fluorescence correlation spectroscopy diffusion laws to probe the submicron cell membrane organization. *Biophys J* 89, 4029–4042.
- Wieser S, Moertelmaier M, Fuertbauer E, Stockinger H, Schutz GJ (2007). (Un)confined diffusion of CD59 in the plasma membrane determined by high-resolution single molecule microscopy. *Biophys J* 92, 3719–3728.
- Wu W, Shi X, Xu C (2016). Regulation of T cell signalling by membrane lipids. *Nat Rev Immunol* 16, 690–701.
- Yu SR, Burkhardt M, Nowak M, Ries J, Petrusek Z, Scholpp S, Schwillke P, Brand M (2009). Fgf8 morphogen gradient forms by a source-sink mechanism with freely diffusing molecules. *Nature* 461, 533–536.
- Yuan CB, Johnston LJ (2001). Atomic force microscopy studies of ganglioside GM1 domains in phosphatidylcholine and phosphatidylcholine/cholesterol bilayers. *Biophys J* 81, 1059–1069.